

## Supporting Information

### **PtNiFe Nanoalloys with Co-existence of Energy-optimized Active surfaces for Synergistic Catalysis of Oxygen Reduction and Evolution**

*Wei Yang<sup>a</sup>, Wenbin Gong<sup>d</sup>, Yanhong Shi<sup>a</sup>, Xiaona Wang<sup>a</sup>, Yulian Wang<sup>a, b</sup>, Jian Qiao<sup>a</sup>, Sha Zeng<sup>a</sup>, Jiangtao Di<sup>a, b, c, \*</sup>, and Qingwen Li<sup>a, b, c, \*</sup>*

<sup>a</sup> Key Laboratory of Multifunctional Nanomaterials and Smart Systems, Advanced Materials Division, Suzhou Institute of Nano-Tech and Nano-Bionics, Chinese Academy of Sciences, Suzhou 215123, China.

<sup>b</sup> School of Nano-Tech and Nano-Bionics, University of Science and Technology of China, Hefei 230026, China

<sup>c</sup> Division of Nanomaterials, Suzhou Institute of Nano-Tech and Nano-Bionics, Chinese Academy of Sciences, Nanchang 330200, China

<sup>d</sup> School of Physics and Energy, Xuzhou University of Technology, Xuzhou 221018, China

#### **Corresponding Author**

Email: [jtdi2009@sinano.ac.cn](mailto:jtdi2009@sinano.ac.cn) (Jiangtao Di), [qwli2007@sinano.ac.cn](mailto:qwli2007@sinano.ac.cn) (Qingwen Li)

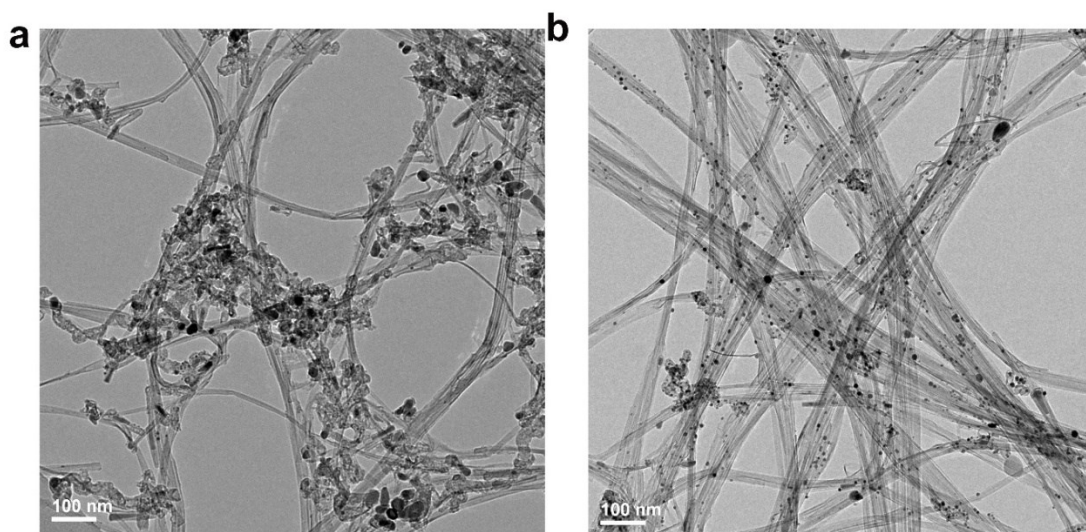


**Figure S1.** The TEM image of Fe-CNTs and Fe-NCNTs.

The Fe-CNTs network prepared by the CVD method contains a large amount of iron particles, and these iron particles with non-uniform size are distributed in the cross-linked CNT network (Figure S1). The Fe-CNTs calcined in  $\text{NH}_3$  gas at  $500^\circ\text{C}$  for 2h (as  $\text{NH}_3$  is a corrosive gas), which not only resulting in the CNTs doped with nitrogen, but also resulting in the size of Fe particles significantly reduced and the distribution more uniform.

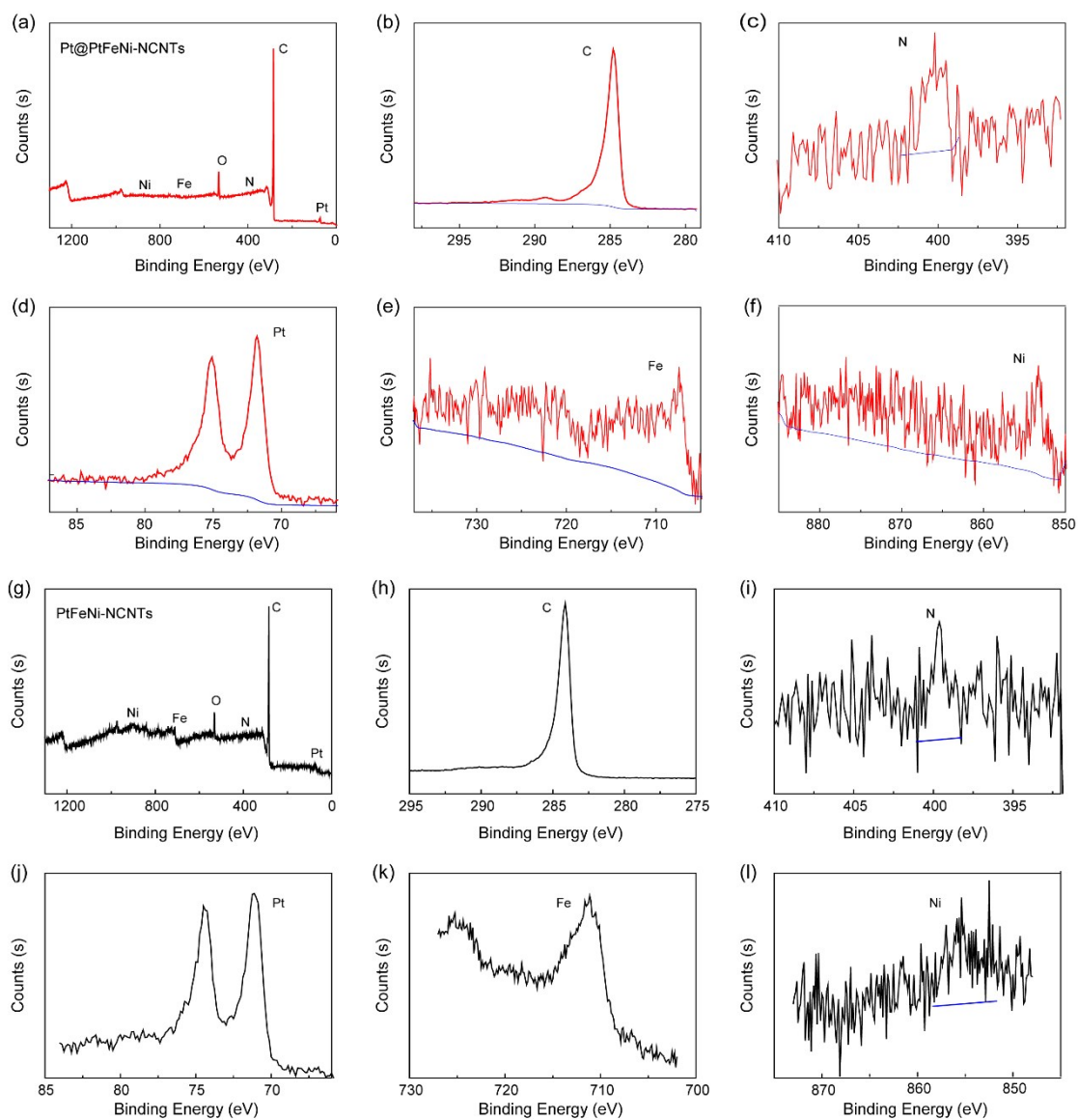


**Figure S2.** The XPS survey spectra of Pt@PtFeNi-NCNTs (a-f) and PtFeNi-NCNTs (g-l).

The XPS survey spectra of Pt@PtFeNi-NCNTs and PtFeNi-NCNTs shown in Figure S2 were used to clearly identify the chemical element composition.

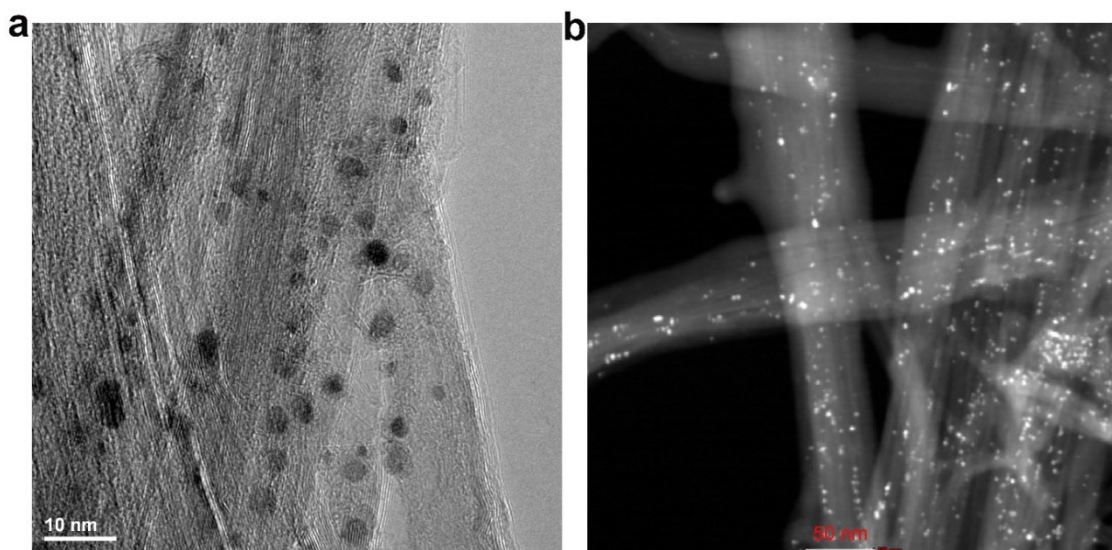


**Figure S3.** (a) TEM image of Pt@PtFeNi-NCNTs, (b) STEM image of Pt@PtFeNi-NCNTs

As shown in S3a, b, the PtFeNi nanoparticles in the Pt@PtFeNi-NCNTs sample were uniform in size (about 2 nm), and they were evenly distributed on the NCNT without agglomeration.

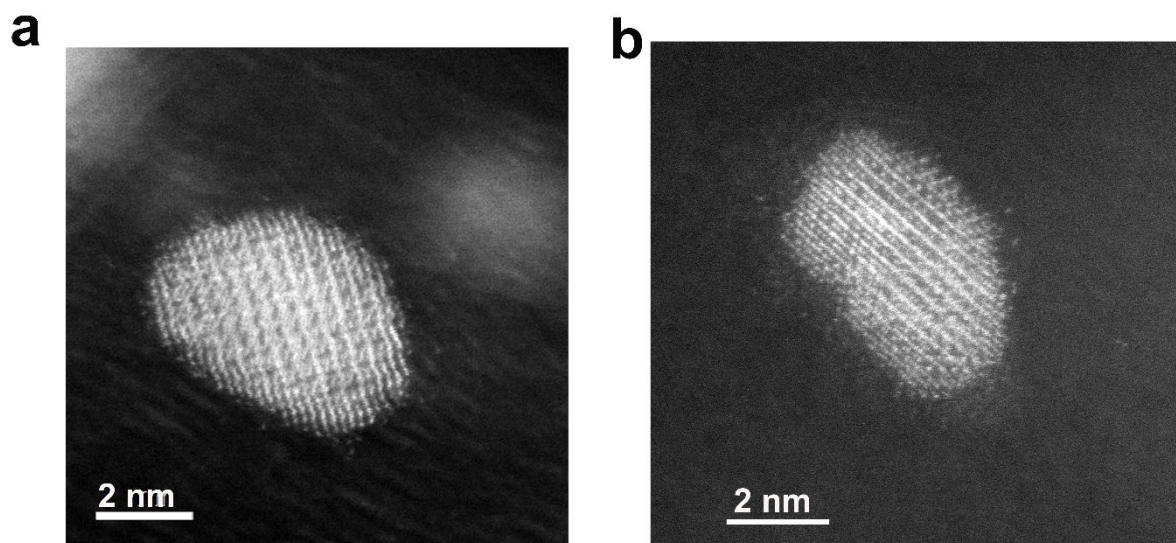


**Figure S4.** Atomic-resolution HAADF-STEM image of Pt@PtFeNi-NCNTs

High- HRTEM revealed that the Pt@PtFeNi-NCNTs had a PtFeNi core and a Pt shell. Apparent ordering of Fe, Ni and Pt in PtFeNi core with facecentered cubic crystal structures was also observed along the  $\langle 100 \rangle$  and  $\langle 110 \rangle$  directions, which supporting the existing of superstructures known to be highly active in the Pt@PtFeNi-NCNTs (Figure S4).

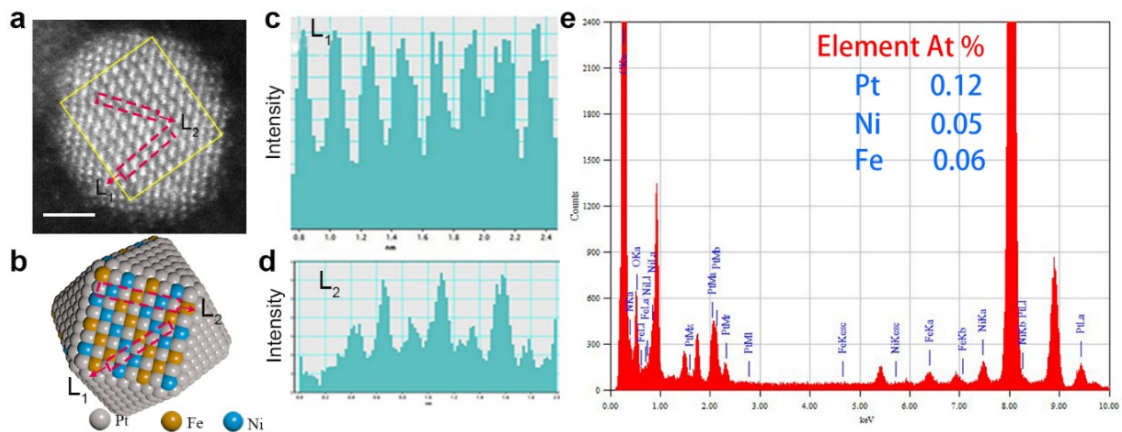


**Figure S5.** (a) Atomic-resolution HAADF-STEM image of Pt@PtFeNi-NCNTs, with the intensity of sites L<sub>1</sub> and L<sub>2</sub>, shown in (c) and (d), (b) Schematic diagram of Pt@PtFeNi-NCNTs, (e) EDS spectrum of Pt@PtFeNi-NCNTs

Unlike the uniform PtFeNi alloy particles, the Pt@PtFeNi-NCNTs sample with core-shell structure had Pt-rich shell and PtFeNi alloy core. The presence of the L<sub>1</sub> and L<sub>2</sub> ordered intermetallic structures of the core of Pt@PtFeNi-NCNTs could be identified by an intensity analysis. The EDS analysis showed that the atom ratios of those elements in the sample were approximately 2:1:1 (Figure S5e), which is in agreement with the ICP analysis.

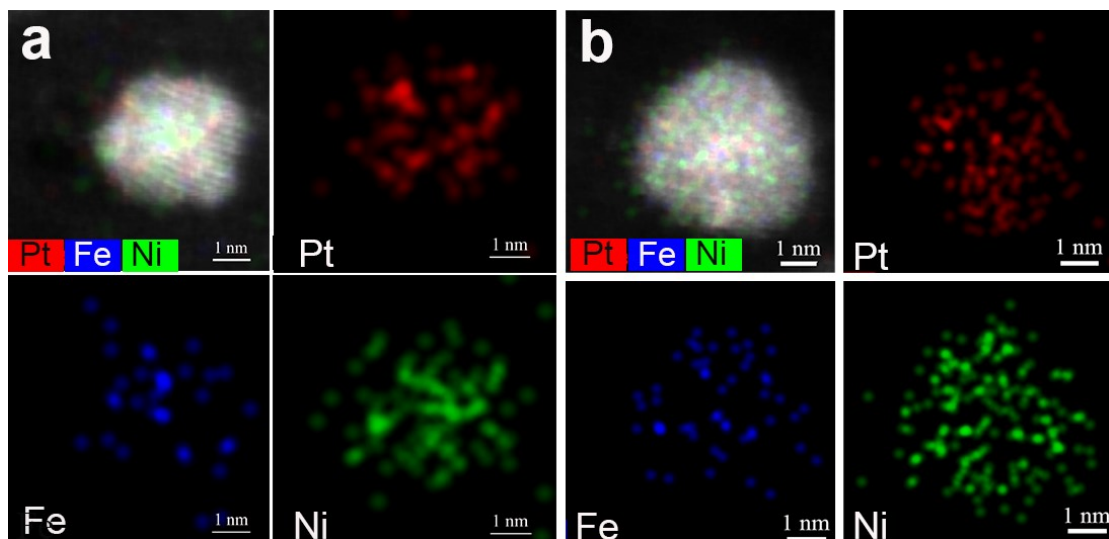


**Figure S6.** Corresponding EDS mapping image of Pt, Fe and Ni elements in (a) Pt@PtFeNi-NCNTs, (b) PtFeNi-NCNTs.

EDS mapping (Figure S6a) further indicated that the elemental compositions of these samples were dominated by Pt, Fe, and Ni. EDS further proves that the Pt@PtFeNi-NCNTs sample had a shell-core structure, most Pt atoms surround the edges of the particles while the Ni and Fe atoms mostly gather in the middle of the nanoparticles. As a comparison, the Pt, Fe, Ni atoms are uniformly distributed throughout the PtFeNi nanoparticles, in Figure S6b.

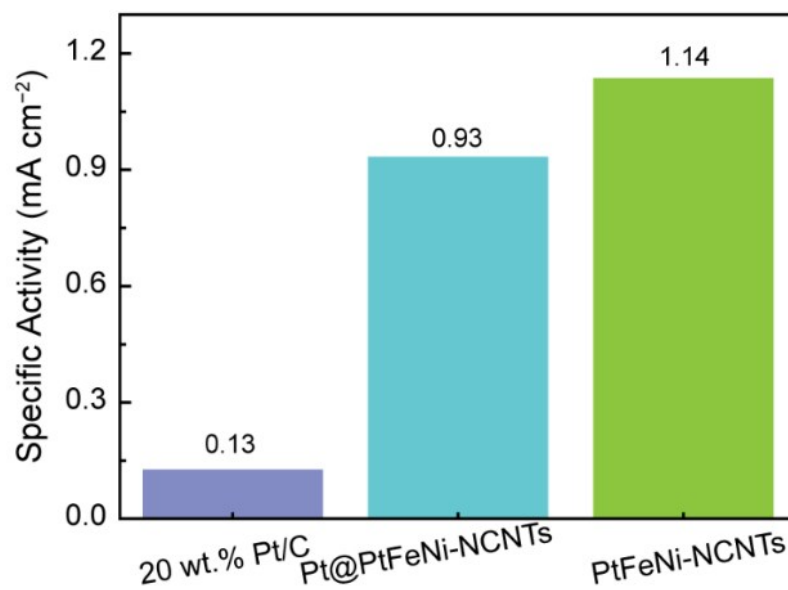


**Figure S7.** Optical image of the freestanding, lightweight, and robust Pt@PtFeNi-NCNTs film.

The specific activity of Pt@PtFeNi-NCNTs was larger than Pt/C and smaller than PtFeNi-NCNTs, indicating that the excellent ORR activity of Pt@PtFeNi-NCNTs attributed to the synergy of larger ECSA and better intrinsic activity.

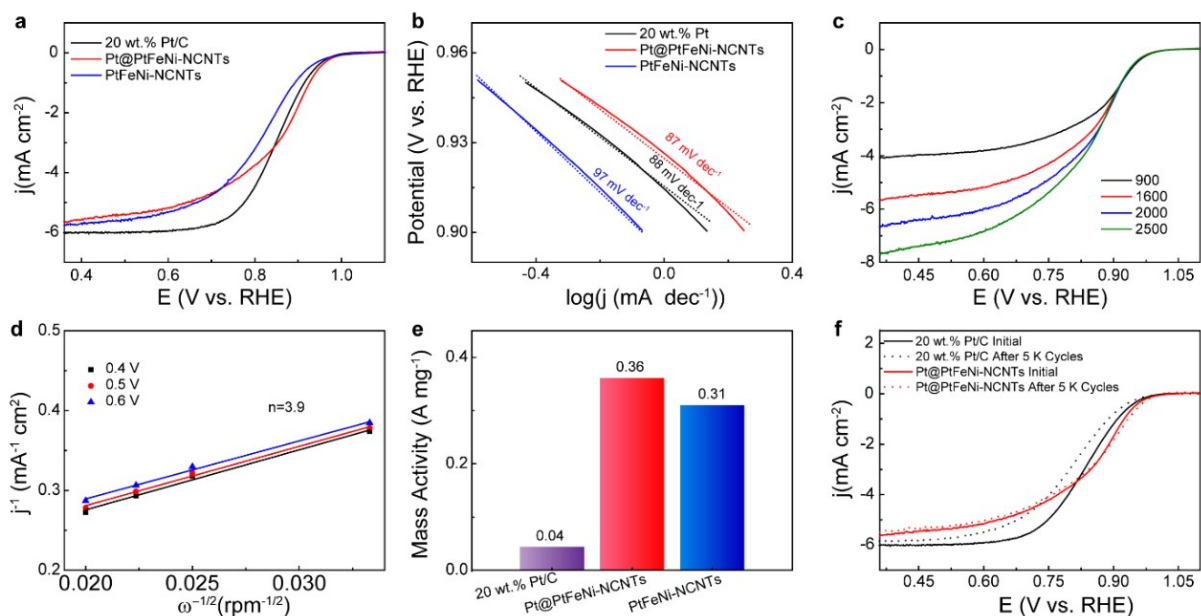


**Figure S8.** (a) ORR LSV curves at 1600 rpm for the catalyst films of 20 wt.% Pt/C, PtFeNi catalysts, and in oxygen-saturated 0.1 M HClO<sub>4</sub> aqueous electrolyte (b) ORR Tafel plots of 20 wt.% Pt/C and PtFeNi catalysts (c) ORR LSV curves at different rotation speed for the Pt@PtFeNi-NCNTs. (d) K-L plots of the Pt@PtFeNi-NCNTs (e) Mass activities of the catalyst of 20 wt.% Pt/C and PtFeNi catalysts (f) Accelerated degradation test on a Pt@PtFeNi-NCNTs catalyst and 20 wt.% Pt/C: CV curves after 5000 cycles at a scan rate of 100 mV s<sup>-1</sup>.

We also appraised the ORR activities of the Pt@PtFeNi-NCNTs and the control groups in O<sub>2</sub>-saturated 0.1 M HClO<sub>4</sub> media. These revealed that the Pt@PtFeNi-NCNTs catalyst is much more activity and stable than the commercial Pt/C catalyst in acidic media.

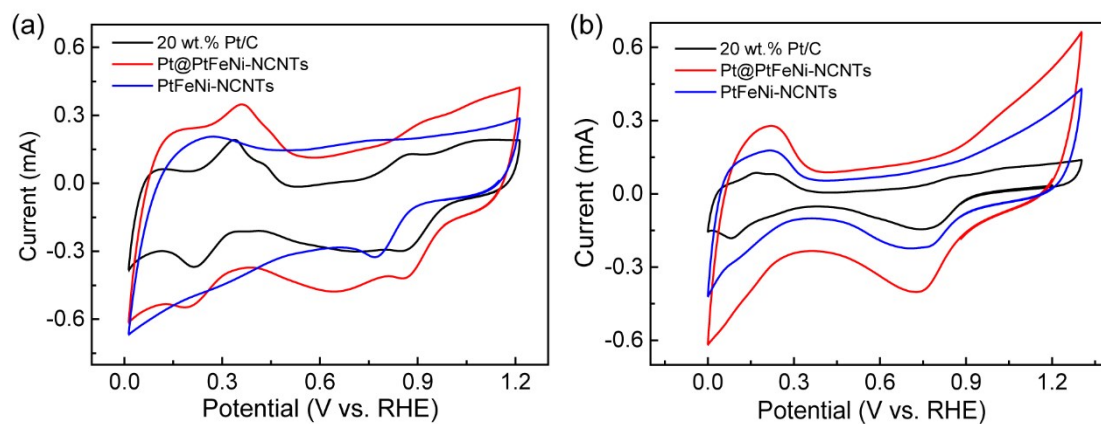


**Figure S9.** CVs of Pt/C, Pt@PtFeNi-NCNTs, and PtFeNi-NCNTs in 0.1 mol L<sup>-1</sup> KOH solution (a) and 0.1 mol L<sup>-1</sup> HClO<sub>4</sub> solution (b).

As shown in Fig. S9 Pt@PtFeNi-NCNTs has the significant redox peak in an O<sub>2</sub>-saturated alkaline and acid solution.

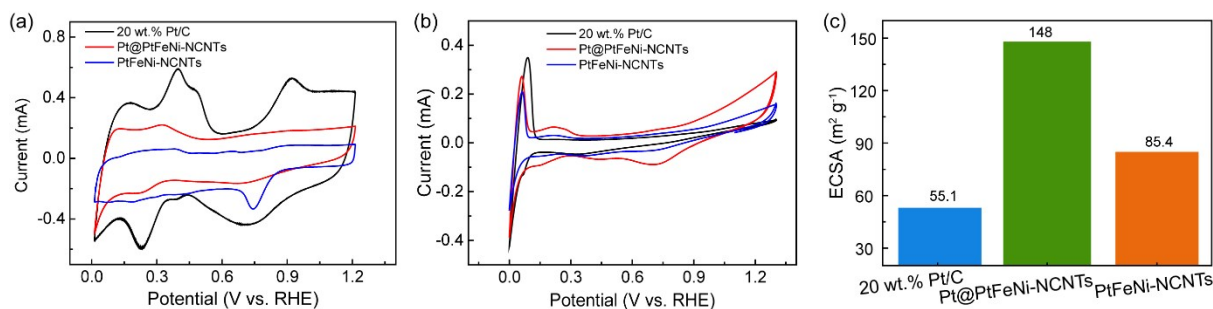


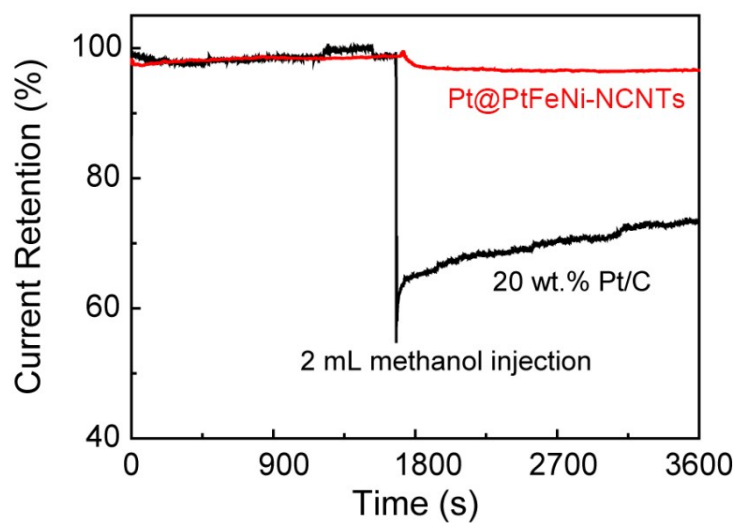
**Figure S10.** CVs of Pt/C, Pt@PtFeNi-NCNTs, and PtFeNi-NCNTs in 0.1 mol L<sup>-1</sup> Ar-saturated KOH solution (a), HClO<sub>4</sub> solution (b), and the ECSA of Pt/C, Pt@PtFeNi-NCNTs, and PtFeNi-NCNTs in acidic solution.

The ECSA is calculated by the following following equation:

$$ECSA = \frac{\frac{S_H}{V}}{0.21(mC * cm^{-2}) * M_{Pt}}$$

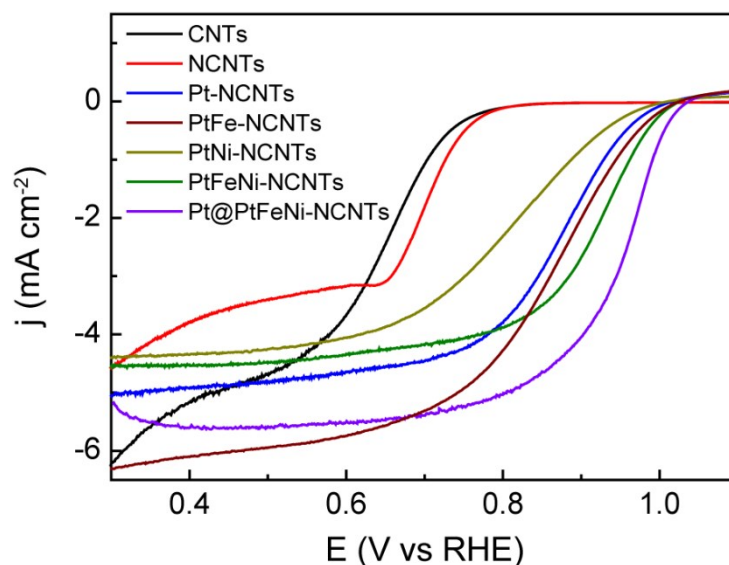
Where  $S_H$  is the peak area,  $V$  is the sweep rate,  $C$  is the cullen and  $M_{Pt}$  is the quality of the Pt (g).

Figure S10 shows the  $H_{UPD}$  areas of Pt/C (20 wt%, JM), Pt@PtFeNi-NCNTs, and PtFeNi-NCNTs in 0.1 mol L<sup>-1</sup> Ar-saturated KOH solution and HClO<sub>4</sub> solution, indicating that the Pt@PtFeNi-NCNTs had a much larger ECSA (148 m<sup>2</sup> g<sup>-1</sup>) than Pt/C (55.1 m<sup>2</sup> g<sup>-1</sup>) and PtFeNi-NCNTs (85.4 m<sup>2</sup> g<sup>-1</sup>) in acidic solution. It can be found from Figure 3d and Figure S10c that the ECSA of Pt@PtFeNi-NCNTs is superior to Pt/C and PtFeni-NCNTs in both acidic and alkaline electrolytes.



**Figure S11.** Resistance to methanol poisoning of the Pt@PtFeNi-NCNTs and 20 wt.% Pt/C catalysts.

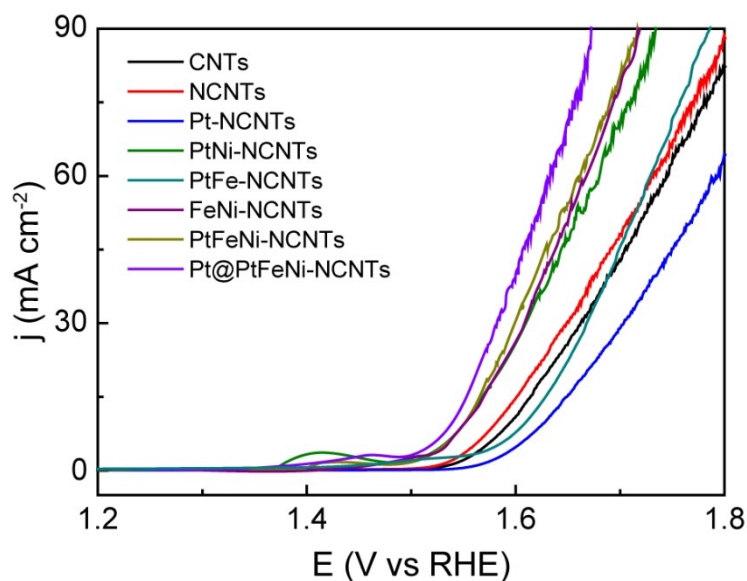
The performance durability was also characterized when the Pt@PtFeNi-NCNTs catalyst and the commercial Pt/C catalyst were exposed to methanol. The current retention of the Pt@PtFeNi-NCNTs catalyst remains almost 100% after methanol injection, whereas the current density retention of the commercial 20 wt.% Pt/C catalyst decreases to approximately 50% after methanol injection.



**Figure S12.** ORR LSV curves at 1600 rpm for the catalysts of CNTs, NCNTs, Pt-NCNTs, PtNi-NCNTs, PtFe-NCNTs and Pt@PtFeNi-NCNTs in oxygen-saturated 0.1 M KOH aqueous electrolyte.

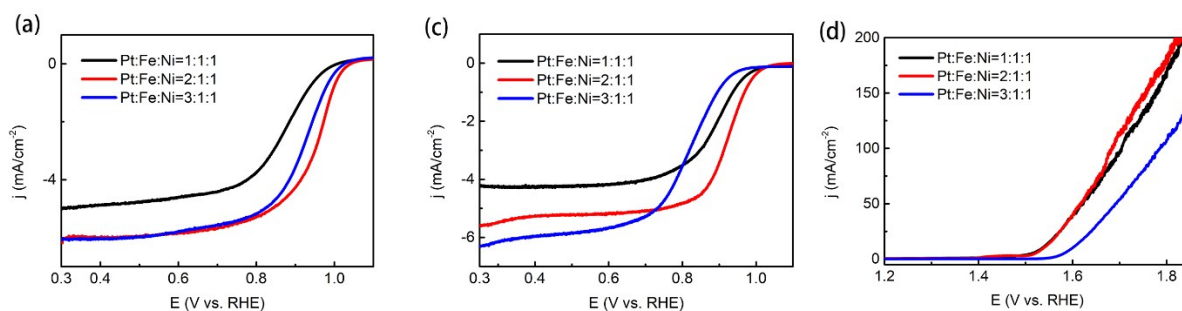
The pristine CNT film was treated at 773 K under an  $\text{NH}_3$  (in 50% Ar) atmosphere for 2 h in a tube furnace at a ramp rate of  $5\text{ }^\circ\text{C min}^{-1}$  to obtain an NCNT film. The Pt-NCNTs, PtNi-NCNTs, PtFe-NCNTs, PtFeNi-NCNTs and Pt@PtFeNi-NCNTs catalysts were prepared by the same method. The corresponding metal salt were dissolved in 2 mL ethanol as a precursor solution. Then the NCNT film was immersed in the precursor solution for 2 h. After dried at room temperature, the sample treated at the annealing temperature of  $1000\text{ }^\circ\text{C}$  under Ar atmosphere for 2 h in a tube furnace at a ramp rate of  $5\text{ }^\circ\text{C min}^{-1}$ . After being cooled naturally to room temperature, the resulting product, the samples were obtained.

It can be seen from Figure S12, that the performance of the ternary alloy is better than that of the monometallic and bimetal catalysts, indicating that there is a synergistic catalytic effect among the ternary metals of Pt, Fe, and Ni. The core-shell Pt@PtFeNi-NCNTs catalyst showed the most excellent catalytic performance compared to monometallic, bimetal catalysts and the ternary metals catalyst, which indicating that the synergistic catalytic effect come from the core-shell structure and the ternary metals.



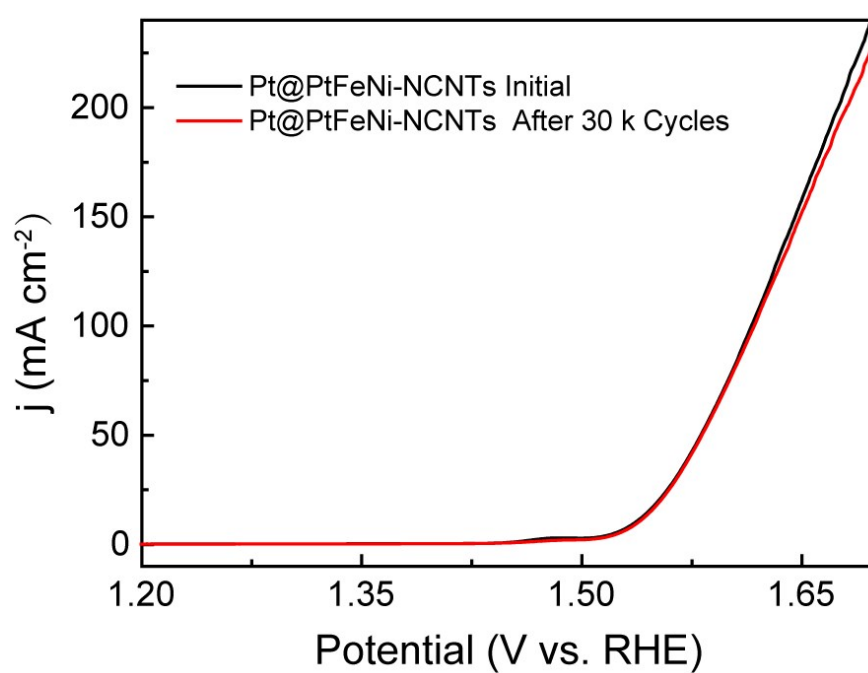
**Figure S13.** OER LSV curves for CNTs, NCNTs, Pt-NCNTs, PtNi-NCNTs, PtFe-NCNTs, FeNi-NCNTs, PtFeNi-NCNTs and Pt@PtFeNi-NCNTs in 1 M KOH aqueous electrolyte.

The catalysts prepared above were also tested for OER performance, and it was found that the OER performance of the ternary alloy as the ORR performance was better than that of the monometallic and bimetallic catalysts, indicating that the ternary metals of Pt, Fe, and Ni also played their role in OER catalysis. The core-shell Pt@PtFeNi-NCNTs catalyst showed the most excellent catalytic performance compared to monometallic, bimetal catalysts and the ternary metals catalyst, which indicating that the synergistic catalytic effect come from the core-shell structure and the ternary metals.



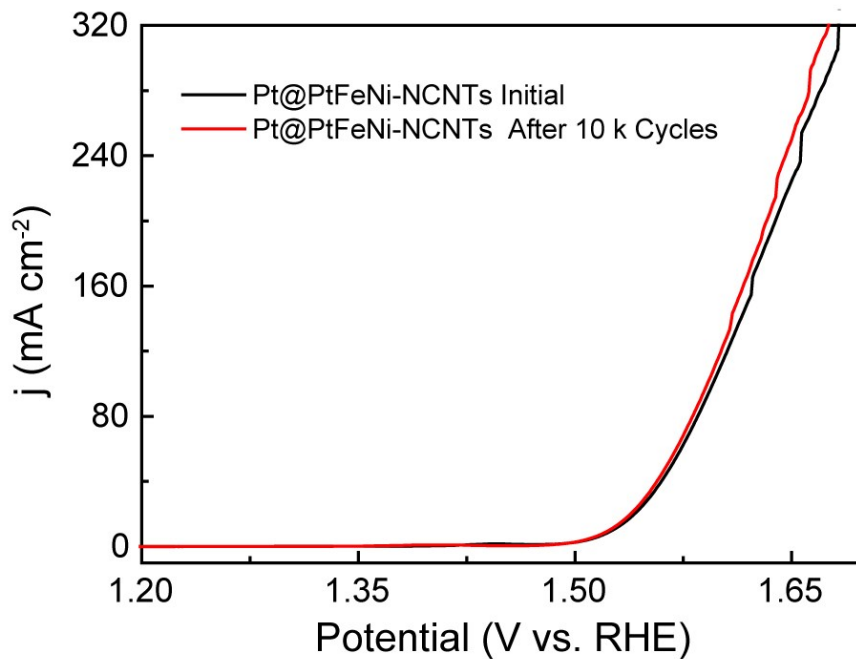
**Figure S14.** (a) ORR LSV curves in an oxygen-saturated 0.1 M KOH aqueous electrolyte. (b) ORR LSV curves in an oxygen-saturated 0.1 M HClO<sub>4</sub> aqueous electrolyte and (c) OER LSV curves for samples with different ratios of platinum to transition metals.

Figure S14 shows the comparison of catalytic activity with different material ratios. The onset potential and half-wave potential of the catalyst with material ratio (Pt:Fe:Ni=2:1:1) of the catalyst described in the experimental part was positively shifted compared to other catalysts with different material ratios (Pt:Fe:Ni=1:1:1 and Pt:Fe:Ni=3:1:1). The result demonstrated the starting material ratio described in the experimental part has the best excellent catalytic performance.



**Figure S15.** Accelerated degradation test by performing CV after 30 K cycles at a scan rate of  $200 \text{ mV s}^{-1}$  on the Pt@PtFeNi-NCNTs catalyst in a  $1 \text{ mol L}^{-1}$  KOH solution.

A six days stability test for the OER was took in  $1 \text{ mol L}^{-1}$  KOH solution. As illustrated in Figure S15, the onset potential and  $E_{j=10}$  of Pt @ PtFeNi-NCNT remained unchanged after 30 K cycles, indicating its excellent catalytic stability for oxygen evolution.



**Figure S16.** Accelerated degradation test by performing CV after 10 K cycles at a scan rate of  $200 \text{ mV s}^{-1}$  on the Pt@PtFeNi-NCNTs catalyst in a  $6 \text{ mol L}^{-1}$  KOH solution.

The stability of the catalyst in  $6 \text{ mol L}^{-1}$  KOH solution encountered in commercial alkaline hydrolysis was considered. As illustrated in Figure S16, the onset potential and  $E_{j=10}$  of Pt@PtFeNi-NCNT exhibited a negligible decrease after 10 K cycles, indicating its excellent catalytic stability and application prospects in commercial alkaline water electrolytes.

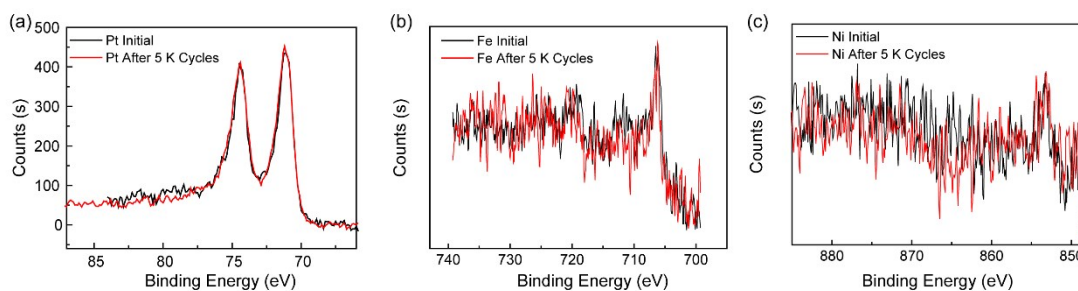


**Figure S17.** High-resolution Pt, Fe, Ni XPS spectra for the Pt@PtFeNi-NCNTs catalysts before and after 5000 cycles.

The XPS analysis on the samples before and after the OER cycle was conducted. It can be seen that the XPS spectrum peak of Pt, Fe, Ni element were almost unchanged, indicating that no new substances were produced, and the catalyst after cycles was still the PtFeNi alloy.



**Figure S18.** Optical image of the freestanding, lightweight and robust Pt@PtFeNi-NCNTs film.

Distinguishing from most of the previously reported power-like catalysts, the as-obtained Pt@PtFeNi-NCNTs film is freestanding and lightweight (Figure S18). The Pt@PtFeNi-NCNTs film such as high electrical conductivity, high mechanical strength, and porous networks, which allow the direct use of the Pt@PtFeNi-NCNTs film as a robust cathode without the need of conventional current collectors and gas diffusion layers.

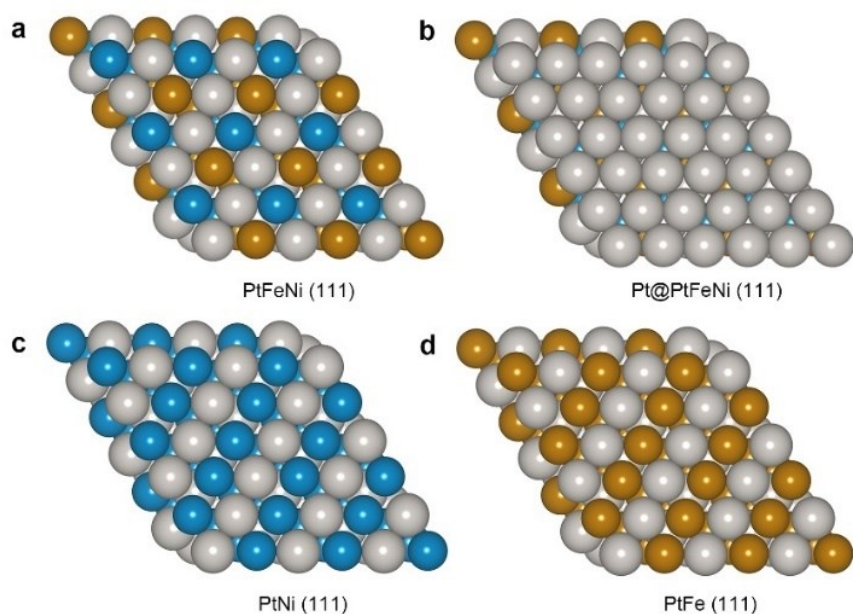


**Figure S19.** The configurations of (111) surface of (a) PtFeNi, (b) Pt@PtFeNi, (c) PtNi and (d) PtFe.

The IMC model was constructed based on the HRTEM observation, with optimized lattice constants of  $3.87 \text{ \AA} \times 3.62 \text{ \AA} \times 3.87 \text{ \AA}$  and (111) surface set spacing of  $2.23 \text{ \AA}$ , which closely corresponded to the experimental results. Notably, the in-plane lattice constant of the IMC (111) surface, which was the most stable surface, is smaller than that of Pt (111) but larger than those of PtNi (111) and PtFe (111).

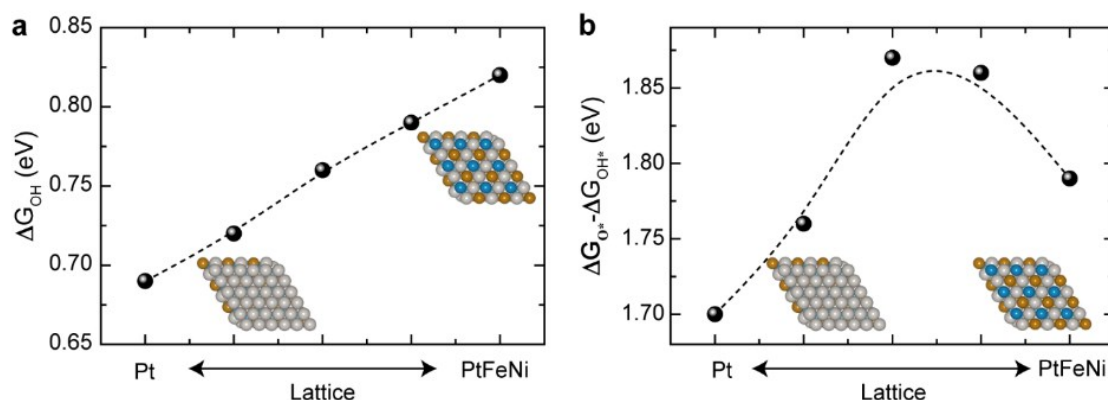


**Figure S20 (a)** Calculated adsorption configurations of the intermediate species OH\* of the ORR on the surfaces of Pt@PtFeNi (111) and PtFeNi (111) and corresponding Gibbs free energy, **(b)** Calculated adsorption configurations of the intermediate species O\* and OH\* of the OER on the surfaces of PtFeNi (111) and corresponding Gibbs free energy.

This lattice mismatch between the core (FeNi-rich) and the surface (Pt-rich) endowed the catalyst with nonuniform stresses on different surfaces. As shown in Figure S20, the non-uniform stresses on different catalyst surfaces were beneficial to the catalytic activity.



**Figure S21 (a)** The contact angles of the pristine catalyst of Pt@PtFeNi-NCNTs, **(b)** The contact angles of the Pt@PtFeNi-NCNTs catalyst after 5 K cycles.

The contact angle of the pristine catalyst (Pt@PtFeNi-NCNTs) compared to one after 5 K cycles were tested by a contact angle measurement. As shown in Figure S21, after 5 K cycles,

the contact angle of the Pt@PtFeNi-NCNTs was significantly reduced, which indicating the increased performance after 5000 cycles was due to increased wettability of the catalyst.